

Models of gravitational lens candidates from Space Warps CFHTLS

Rafael Küng,¹ Prasenjit Saha,¹ Ignacio Ferreras,² Elisabeth Baeten,³ Jonathan Coles,⁴ Claude Cornen,³ Christine Macmillan,³ Phil Marshall,⁵ Anupreeta More,⁶ Lucy Oswald⁷ Aprajita Verma⁸ and Julianne K. Wilcox³

¹Physik-Institut, University of Zurich, Winterthurerstrasse 190, 8057 Zurich, Switzerland

²Mullard Space Science Laboratory, University College London, Holmbury St Mary, Dorking, Surrey RH5 6NT, UK

³Zooniverse, c/o Astrophysics Department, University of Oxford, Oxford OX1 3RH, UK

⁴Physik-Department, Technische Universität München James-Franck-Str. 1, 85748 Garching, Germany

⁵Kavli Institute for Particle Astrophysics and Cosmology, Stanford University, 452 Lomita Mall, Stanford, CA 94035, USA

⁶Kavli IPMU (WPI), UTIAS, University of Tokyo, Kashiwa, Chiba 277-8583, Japan

⁷Murray Edwards College, University of Cambridge, Cambridge CB3 0DF, UK

⁸Sub-department of Astrophysics, University of Oxford, Denys Wilkinson Building, Keble Road, Oxford, OX1 3RH, UK

Accepted XXX. Received YYY; in original form ZZZ

ABSTRACT

We report modelling follow-up of recently-discovered gravitational-lens candidates in the Canada France Hawaii Telescope Legacy Survey. Lens modelling was done by a small group of specially-interested volunteers from the Space Warps citizen-science community who originally found the candidate lenses. Models are categorised according to seven diagnostics indicating (a) the image morphology and how clear or indistinct it is, (b) whether the mass map and synthetic lensed image appear to be plausible, and (c) how the lens-model mass compares with the abundance-matched halo mass derived from photometry of the lensing galaxy.

The lens-model masses range from $\sim 10^{11} M_{\odot}$ to $> 10^{13} M_{\odot}$. Preliminary estimates of the stellar masses show (with two outliers) a smaller spread in stellar mass: a factor of a few below or above $\sim 10^{11} M_{\odot}$. That is, the stellar-mass fraction declines sharply as total mass increases. The highest-mass system with a convincing model is J1434+522 (SW05). The two low-mass outliers are J0206-095 (SW19) and J2217+015 (SW42); if these two are indeed lenses, they are probing an interesting regime of very low star-formation efficiency.

Some improvements to the modelling software used (SpaghettiLens), and discussion of strategies for scaling to future surveys with more and frequent discoveries, are also included.

Key words: gravitational lensing: strong – galaxies: general

1 INTRODUCTION

By coincidence, the typical escape velocity of massive galaxies is such that v_{esc}^2/c^2 is comparable to the apparent sizes of galaxies at cosmological distances. This coincidence is fortunate, because it makes the lensing deflection angle (which is $2v_{\text{esc}}^2/c^2$) of distant galaxies comparable to their size on the sky, and as a result, strong lensing by galaxies tends to produce images that probe the dark halos of those galaxies. This is important, because while there is a general consensus that basic mechanism of galaxy formation involves gravitational collapse, fragmentation, and mergers of dark-matter clumps, into which gas fell, cooling through radiative processes to

form dense clouds and eventually stars, there is much debate about the details (for a summary, see [Silk & Mamon 2012](#)). In particular, the nature of dark matter remains mysterious: most researchers take it to be a collisionless non-relativistic fluid (cold dark matter or CDM) readily studied by simulations (for example, the influential millenium simulation by [Springel et al. 2005](#)). But other scenarios, where dark matter has exotic dynamical properties ([Saxton & Ferreras 2010](#); [Schive et al. 2016](#)), or is not really matter at all but a modification of gravity ([McGaugh et al. 2016](#)), have also been considered.

All this motivates using galaxy lenses to study the mutual dynamics of dark matter, gas and stars in galaxies.

Several studies in recent years have done so (Koopmans et al. 2009; Leier et al. 2011, 2012, 2016; Bruderer et al. 2016) but it is desirable to enlarge the samples from tens of lensing galaxies to thousands. Doing so requires both finding more lenses and also modelling their masses. Recent searches through the CFHTLS (Cuillandre et al. 2012) using arc-finders (e.g., More et al. 2012; Maturi et al. 2014; Gavazzi et al. 2014) by machine learning (e.g., Paraficz et al. 2016; Lanusse et al. 2017) and by visual inspection by citizen-science volunteers in Space Warps (More et al. 2016) have, between them, discovered an average of four lenses per square degree, so one can be optimistic about finding many thousands of lenses in the next generation of wide-field surveys, from the LSST in optical and the SKA in radio on the ground, and Euclid andWFIRST in orbit.

The expected flood of new lens discoveries will need a similarly huge modelling effort to reconstruct their mass distributions. To prepare for the challenge of massive-sample lens modelling, Küng et al. (2015) developed a new modelling strategy, implemented as the SpaghettiLens system. The idea is to collaborate with experienced members of the citizen-science community, who have already participated in lens discovery through Space Warps, as well as several other projects involving astronomical data. The system was tested on a sample of simulated lenses, which were part of the training and testing set in Space Warps.

This paper continues that study by applying SpaghettiLens to lens-candidates discovered through Space Warps. We present results from modelling of 56 of the 59 lens candidates reported by More et al. (2016). Each lens candidate was modelled in a collaborative refinement process, where anyone interested can create a new model or modify an existing model to try and make it better.¹ The result model represents a consensus among contributors, as to the best that could be achieved with the available data and software.

We characterise each model with seven diagnostics, grouped into three categories, whose purpose is to help identify which systems are most probably lenses, and which ones are likely to be most rewarding for future follow-up observations. The diagnostics are as follows.

- First we have diagnostics based on morphology of the system. Section 2 and Figure 1 explain.

- Whether the images are unblended. Distinct unblended images are an advantage in modelling, but not essential.

- Whether all images are discernible. The topography of an arrival-time surface, as encoded by a spaghetti diagram, may require more images than are visible, in which case the modeller has to insert conjectural image positions.

- Whether the lens is fairly isolated.
- The image morphology concisely described: double or

¹ This is in contrast to the main Space Warps project for discovering lenses, where volunteers in a crowd of $\gtrsim 10^4$ make independent contributions. Each person is presented with a random selection of survey-patches and invited to (in effect) vote on each. The system estimates each volunteer’s skill level according to test-patches interspersed with the real data, and weights their votes accordingly (Marshall et al. 2016). There is an active forum for volunteers, but since everyone is seeing different data samples with minimal overlap, the forum has little if any influence on votes.

quads, further sub-categorised to indicate the elongation direction of the lensing mass.

- Second we have mass models, covered in Section 3.
 - Whether the mass map is reasonable. Figure 4.
 - Whether the arrival-time surface and synthetic image are plausible. In particular, additional images are implied in regions where they are not observed signal an unsatisfactory model. Figures 2 and 3 and 5.
 - Third, whether the implied lensing mass is plausible, given the photometry of the lensing galaxy. Section 4 explains how we compare the lensing mass with the mass in stars in the lensing galaxy. We estimate the stellar mass by comparing galaxy magnitudes from the CFHTLS pipeline with the well-known stellar-population models of Bruzual & Charlot (2003). We then extrapolate the stellar mass to a halo mass using the abundance-matching prescription of Moster et al. (2010). Naturally, the lensing mass must be more than the stellar mass but no more than the total halo mass. We then introduce what we call a halo index (\mathcal{H}) which gives an idea of how the lensing mass compares with these two constraints. Figure 6.

Section 5 summarises and tabulates the diagnostics in Table 1. Interpretation of the results is tentative, because the systems are lens candidates at this stage, not secure lenses. Moreover the candidate-lens redshifts have large uncertainties, while the candidate-source redshifts can only be guessed at present. Nevertheless it is interesting to see what trends we can observe with the already-available data.

There are three appendices devoted to various technical issues relating to modelling. Küng et al. (2015) tested the system on simulated lenses and identified some areas for improvement. In § A1 we introduce fitting of the brightness profiles of the source. This feature has not yet been included in SpaghettiLens, but has been carried out in post-processing for a few especially interesting candidates. In § A2 we show that making mass maps fine-grained in the central region relieves a tendency in the earlier work for mass profile to be too shallow. Then in § A3 we consider the possibility of fitting a parametric lens model to the model ensemble; so far we have only been successful at extracting an Einstein radius.

The online supplement gives results for all the modelled systems generated for all the lensing candidates.

2 IMAGE MORPHOLOGY

A modeller’s main input to the lens-modelling process is a markup of the candidate lens system, which we call a spaghetti diagram. This is a sketch of the arrival-time surface from a point-like source, with proposed locations of maxima, minima and saddle points, and an implied time-ordering of the images. Such information encodes a starting proposal for the mass distribution. A spaghetti diagram is thus a completely abstract construction, and moreover it refers to a simplified system with a point source. However, spaghetti diagrams are intuitive because they tend to resemble the form of lensed arcs, and of course they are simple to draw, and easy to vary and refine in an open collaborative environment. This makes them very practical for non-professional lens

enthusiasts in the citizen-science community. Details and tests are given in [Küng et al. \(2015\)](#).

We now discuss the diagnostics that can be taken from the process of drawing the spaghetti diagram, even before detailed mass-modelling takes place. Figure 1 shows nine examples, each consisting of a cutout of the Space Warps image of a lens candidate, marked up with a spaghetti diagram.

All the examples in Figure 1 identify five locations: the centre of the main lensing galaxy, which is also a maximum of the arrival time surface (red dots); two minima (blue dots); and two saddle points (green dots and also self-intersections of the curves). Only two (SW05 and SW42) of the nine systems, however, have five distinct features in plausible locations. In the other seven examples, an arc is interpreted as a blend of three or four images. This gives the ‘unblended images’ diagnostic. Note that this characterisation could be different if the spaghetti diagram is different. For example, SW28 has also been modelled with the arc on the right interpreted as a single image, rather than as three images as shown in the figure; for such a model, ‘unblended images’ diagnostic would be true.

The second diagnostic is whether all images are visible. For example, we see in SW58 at the top left of Figure 1 that an image at the second minimum is conjectural and does not correspond to any visible feature.

The third diagnostic is whether the lens is fairly isolated, or whether there are other galaxies in the field that probably contribute significantly to the lensing. For this, we do not consider stars or other clearly foreground objects. Additional galaxies contributing to the lensing mass can be marked by the volunteer alongside the spaghetti diagrams. An example can be seen as the grey dot and circle in the cutout with SW57 at the top right of Figure 1. Objects marked in this way are modelled as point masses. Other possible contributors to lensing are galaxies or groups that are not in the immediate vicinity of the lensed images, yet massive enough to have an effect. These are accounted for by allowing a constant but adjustable external shear.

We remark that blended images or missing images or perturbing galaxies do not imply that a given candidate is unlikely to be a lens. They mean, rather, that the models are more uncertain and perhaps could be more easily improved by trying further variations in the markup.

The fourth diagnostic is based on the fact that the arrangement of lensed images of a pointlike source through a non-circular gravitational lens depends on the location of the source relative to the long and short axes of the lens. This dependence is quite robust and independent of many other details of the lensing mass distribution. Sources close to being dead-centre behind a lens tend to produce quads, sources at larger transverse distance tend to produce doubles. We denote these as Q and D respectively, and add a prefix to the Q systems, as follows: we write LQ if the source is inferred as displaced along the long axis of the lens, SQ if displaced along the short axis, IQ if inclined to both axes, CQ if only very little to no inclination. Although the unlensed source and its location are obviously not seen, the LQ, SQ, IQ and CQ cases correspond to easily-seen image morphologies (see, e.g., [Saha & Williams 2003](#)).

- The simplest is the SQ case: this creates a saddle point and two minima in an arc, with the second saddle point on

the other side of the lensing galaxy, and closer to the galaxy than the arc is. SW58 and SW28 in the upper row of Figure 1 are typical examples of SQ.

- The middle row of Figure 1 shows three IQ systems, SW05, SW42 and SW19. This type has a characteristic asymmetry, often with two images close together.

- The lower row of Figure 1 shows three LQ systems, SW09, SW29 and SW02, and the failed model SW57 at top right also possibly belonging to this category. Here the images have a fairly symmetric arrangement with an arc and a counter-image on the other side, but the spaghetti diagram is completely asymmetric. LQ can be visually distinguished from SQ from the relative distances of the arc and the counter-image. For LQ the arc is closer, for SQ the counter-image is closer.

Although the labels ‘short-axis quad’ and so on are not standard in the literature, the morphological classification they express is familiar to experienced modellers. Hence they can be useful to researchers wishing to apply other modelling methods to the same systems.

3 MASS MODELS

Once a spaghetti diagram has been drawn on a web browser, it is forwarded to a server-side numerical framework, which searches for mass maps consistent with the given image locations, parities and time ordering. The mass maps are made up of mass tiles and are free-form, but are required to be concentrated around the identified lens centre (see [Coles et al. 2014](#), for the precise formulation of the search problem.) Assuming such mass distributions can be found (which in practice is usually the case) a statistical ensemble of two-dimensional mass maps is returned. This ensemble, along with derived quantities and uncertainties, makes up one SpaghettiLens model.

The mass will naturally depend on the lens and source redshifts, which are unknown when a lens candidate is first identified. But this is not a problem, because a model can be trivially rescaled to use better redshift values, as and when they become available. This work applies photometric redshifts from the CFHTLS pipeline to the candidate lensing galaxies; the values range from $z = 0.2$ to $z = 1$ (see Table 1). As the mass normalisation depends only weakly on source redshift, provided it is larger than to the lens redshift, we assumed all sources to lie at $z = 2$ unless an unambiguous photometric redshift is available.

The ensemble of mass maps can be post-processed in many different ways. Four different graphical quantities are particularly useful.

Figure 2 shows arrival-time surfaces corresponding to the spaghetti diagrams in Figure 1. The arrival-time contours look like machine-made elaborations of the input spaghetti diagrams. If the saddle-point contours in the arrival time are qualitatively the same as the curves in the spaghetti diagram (the detailed shape of the spaghetti curves is unimportant), it immediately suggests a successful model. On the other hand, if the arrival-time surface has unexpected minima or saddle points, and especially if the unexpected features are far from identified lens images, that signals a doubtful model. Figure 3 shows what we call synthetic images, meaning reconstructions of the extended lensed features by fitting for

a source. These were generated by a new method, explained in Appendix A1, implemented in offline post-processing after the modelling process was complete. The synthetic images provided by SpaghettiLens during the collaborative modelling and discussion were more crude; these are included in the online supplement.

The arrival-time surface and synthetic image are summarised by one diagnostic, the most important of all: are the lensed features satisfactorily reproduced? This diagnostic remains a judgment call by modellers. A useful quantitative criterion for whether the synthetic image is consistent with the data would need to allow for PSF dependence and unmodelled substructure —otherwise all models would be summarily rejected—and it is not clear how to do this.

Figure 4 shows projected mass maps of the example systems. Actually, this figure only shows the ensemble-average mass maps, and not the variation within the ensemble, from which uncertainties can be inferred. (The same applies to the arrival-time surfaces and synthetic images in the two previous figures. Uncertainties will be shown in a concise form later, with Figure 5.) Figure 4 makes evident the tiled nature of the mass model. The tiles can be smoothed over by interpolating, and this was actually done in the mass maps shown online during the modelling process. It is interesting, however, to see the tiling artifacts, if only as a reminder that the substructure in the mass distribution are very uncertain, even if some integrated quantities are very well constrained. How the free-form mass maps relate to parameterised lens models is discussed in Appendix A3. Note that the arrival-time surface does not have discontinuous jumps, because the modelling numerics uses an analytical integral over square tiles; likewise the lens equation.

Figure 5 shows the enclosed-mass profiles, expressed as the average convergence κ within circles of given projected radius. This time, uncertainties are included. Appendix A2 describes improvements made since our earlier work (Küng et al. 2015), to allow for steeper profiles in the inner regions. The enclosed mass is typically best constrained at the national Einstein radius, becoming more uncertain at larger and smaller radii.

The mass maps and mass profiles are the basis of a further diagnostic: are the mass distributions plausible?

4 STELLAR AND HALO MASS ESTIMATES

The stellar masses of the lens galaxies are derived by comparison of the photometric data with M/L estimates from population synthesis models. In principle, a detailed analysis of the spectral energy distribution is needed to derive accurate stellar masses (e.g. Gallazzi & Bell 2009; Taylor et al. 2011). However, estimates to within 0.3 dex in $\log(M_{\text{stel}}/M_{\odot})$ can be derived with a single colour, preferably tracing a rest-frame colour similar to $U - V$ (see Fig. 1 of Ferreras et al. 2008).

In this paper we further simplify the analysis by assuming a relationship between the apparent total magnitude and stellar mass, at the redshift of the lens. For typical stellar-population parameters, the variation of this relation is at most 1 dex. A further possible systematic error is contamination of the light of the lensing galaxy by the lensed background galaxy. Reducing or eliminating the latter would

require detailed fitting of light distributions for each candidate (see Leier et al. 2011), which we have not yet attempted. Nonetheless, because the lensing masses range over two orders of magnitude, it is still interesting to compare with very rough stellar masses.

We make use of the Bruzual & Charlot (2003) models to derive two functional forms of the stellar mass with respect to SDSS-*i* band magnitudes. The models have solar metallicity, with a Chabrier IMF, and assume two different age trends: a “young” model, with a constant 500 Myr age at all redshifts, and an “old” model where the age is the oldest one possible at each redshift, adopting a standard Λ CDM model with $H_0 = 70 \text{ km s}^{-1} \text{ Mpc}^{-1}$ and $\Omega_m = 0.3$.

Figure 6 shows a comparison of stellar and total masses. The comparatively large uncertainty in the stellar mass will be improved in future work by using available optical and NIR magnitudes to derive more accurate constraints on the stellar populations.

In addition, we also derive halo masses for the lenses using an abundance-matching formula. This technique matches the distribution function of observed stellar mass in galaxies with that of dark-halo masses in N -body simulations to derive a simple relation between stellar mass and halo mass. We emphasize that a halo mass from abundance matching should be considered an “average” estimate, and a significant scatter can be expected as galaxies with the same stellar mass can be found in different environments. We refer the reader to Leier et al. (2012) for an assessment of the effect of abundance matching on the derivation of dark matter halo properties in lensing galaxies. We follow the prescription of Moster et al. (2010), namely:

$$\frac{M_{\text{stel}}}{M_{\text{halo}}} = \frac{2C_0}{(M_{\text{halo}}/M_1)^{-\beta} + (M_{\text{halo}}/M_1)^{\gamma}} \quad (1)$$

$$C_0 = 0.02820, \quad M_1 = 10^{11.884} M_{\odot}$$

$$\beta = 1.057, \quad \gamma = 0.556.$$

Figure 6 may be compared with Figure 4 in More et al. (2011).

The comparison of lensing and stellar masses provides us with the last of our model diagnostics. This is a halo-matching index:

$$\mathcal{H} = \frac{\ln(M/M_{\text{stel}})}{\ln(M_{\text{halo}}/M_{\text{stel}})} \quad (2)$$

that relates the observed lensing to stellar mass, with the global ratio expected if the host halo corresponds to the average value derived by abundance matching. Several cases for \mathcal{H} can be considered:

- $\mathcal{H} < 0$ is unphysical because $M < M_{\text{stel}}$.
- $\mathcal{H} = 0$ is when the stellar mass exactly accounts for the lensing mass.
- $0 < \mathcal{H} < 1$ is the typical situation, where the lens includes stars and dark matter, but not the full halo.
- $\mathcal{H} = 1$ means that the lens consists of the entire halo.
- $\mathcal{H} > 1$ is in tension with abundance-matching, because the lensing mass exceeds the expected halo mass.

The halo-matching index expresses whether the lensing mass is plausible given the light from the candidate lensing galaxy.

5 SUMMARY AND CONCLUSIONS

We report on a first set of mass distributions and follow up diagnostics for the Space Warps lens candidates created with a novel approach that aims to be scalable by orders of magnitudes to prepare for the many thousands of lenses the next generation of wide field surveys will yield.

The way of discovering lenses is changing with the introduction of machine learning and citizen science, combined with the coverage of huge areas by modern surveys. The way mass models also needs to change, in order to be prepared for the increasing influx of lenses to be modelled. This work is a hybrid of the classical style, where a small team of experts invest many hours into the creation of a single model, with the approach of citizen science, where a crowd of amateur volunteers make independent contributions. We are a collaboration of professionals and experienced citizen-science volunteers, aiming to create early-stage lens models as soon as a lens candidate is found.

To assist volunteer modellers assessing their models, we introduce a set of diagnostics allowing the qualification of the lenses and the generated models and present them alongside the generated models. At a later stage, we encourage modellers to apply those diagnostics themselves to get a preliminary feedback on the plausibility of their models.

Table 1 is a summary of our results. It characterises each modelled system with seven diagnostics, indicating (a) the image morphology and how clear or indistinct it is, (b) whether the mass map and synthetic lensed image appear to be plausible, and (c) how the model mass compares with the estimated stellar and full-halo masses. Missing entries are due to photometry data not being available, whereas missing rows are due to models not having been created for this particular candidate.

Figure 6 is another summary. It shows most of the candidates having stellar and total mass typical of massive ellipticals. SW05 is one of the most massive of all the candidates, with a mass of galaxy-group scale. It is a particularly attractive system for follow-up observations at higher resolution, as it is a large system with clear multiple-image features, and modelling leaves little doubt that it is a lens. SW04 seems to be even more massive, but the diagnostics leave some doubts about this model. The two lowest-mass systems, SW19 and SW42, are important if they are indeed lenses, as they would be low-mass lenses dominated by dark matter. All the modelled systems have reasonable stellar-mass fractions, except for two cases where the stellar-mass fraction is too low (halo-matching index > 1): these are SW42 and SW57. In the case of SW57, the model has poor diagnostics and should be discounted. The model for SW42, on the other hand, is quite convincing — except for the high halo-matching index. If SW42 turns out not to be a lens, that would support the halo-matching index as an effective criterion for filtering models.

The trend in Figure 6, that higher-mass galaxies get progressively more dark-matter dominated, is expected, e.g. see Ferreras et al. (2005), as is the span of about one order of magnitude for the stellar mass and the two order of magnitudes for the total mass. With future data, it would be interesting to compare enclosed stellar and total mass as a function of radius, going from star-dominated inner regions to dark halos. Leier et al. (2011) illustrate this behaviour in

their Figure 5, but the present sample could go an order of magnitude higher in mass.

The quick creation of many models for the Space Warps candidates successfully showed that a subset of citizen scientists are interested in being involved in more challenging tasks that take some time to learn. A next steps involves recruiting more lensing enthusiasts, as soon as the next round of Space Warps is started. In the meantime, the improvements shown in the Appendix have to be integrated into regular SpaghettiLens usage. Additionally, photometric fitting could be integrated into SpaghettiLens. This would allow experienced citizen scientists to generate photometric redshifts and stellar masses, and thus generate preliminary dark-matter maps as soon as a lens-candidate is identified.

REFERENCES

- Bruderer C., Read J. I., Coles J. P., Leier D., Falco E. E., Ferreras I., Saha P., 2016, *MNRAS*, **456**, 870
 Bruzual G., Charlot S., 2003, *MNRAS*, **344**, 1000
 Coles J. P., Read J. I., Saha P., 2014, *MNRAS*, **445**, 2181
 Cuillandre J.-C. J., et al., 2012, in Observatory Operations: Strategies, Processes, and Systems IV. p. 84480M, doi:[10.1117/12.9255584](https://doi.org/10.1117/12.9255584)
 Ferreras I., Saha P., Williams L. L. R., 2005, *ApJ*, **623**, L5
 Ferreras I., Saha P., Burles S., 2008, *MNRAS*, **383**, 857
 Gallazzi A., Bell E. F., 2009, *ApJS*, **185**, 253
 Gavazzi R., Marshall P. J., Treu T., Sonnenfeld A., 2014, *ApJ*, **785**, 144
 Keeton C. R., 2001, ArXiv: astro-ph/0102341,
 Koopmans L. V. E., et al., 2009, *ApJ*, **703**, L51
 Künig R., et al., 2015, *MNRAS*, **447**, 2170
 Lanusse F., Ma Q., Li N., Collett T. E., Li C.-L., Ravankhah S., Mandelbaum R., Poczos B., 2017, preprint, [arXiv:1703.02642](https://arxiv.org/abs/1703.02642)
 Leier D., Ferreras I., Saha P., Falco E. E., 2011, *ApJ*, **740**, 97
 Leier D., Ferreras I., Saha P., 2012, *MNRAS*, **424**, 104
 Leier D., Ferreras I., Saha P., Charlot S., Bruzual G., La Barbera F., 2016, *MNRAS*, **459**, 3677
 Marshall P. J., et al., 2016, *MNRAS*, **455**, 1171
 Maturi M., Mizera S., Seidel G., 2014, *A&A*, **567**, A111
 McGaugh S. S., Lelli F., Schombert J. M., 2016, *Physical Review Letters*, **117**, 201101
 More A., Jahnke K., More S., Gallazzi A., Bell E. F., Barden M., Häußler B., 2011, *ApJ*, **734**, 69
 More A., Cabanac R., More S., Alard C., Limousin M., Kneib J.-P., Gavazzi R., Motta V., 2012, *ApJ*, **749**, 38
 More A., et al., 2016, *MNRAS*, **455**, 1191
 Moster B. P., Somerville R. S., Maulbetsch C., van den Bosch F. C., Macciò A. V., Naab T., Oser L., 2010, *ApJ*, **710**, 903
 Paraficz D., et al., 2016, *A&A*, **592**, A75
 Saha P., Williams L. L. R., 2003, *AJ*, **125**, 2769
 Saxton C. J., Ferreras I., 2010, *MNRAS*, **405**, 77
 Schive H.-Y., Chiueh T., Broadhurst T., Huang K.-W., 2016, *ApJ*, **818**, 89
 Silk J., Mamon G. A., 2012, *Research in Astronomy and Astrophysics*, **12**, 917
 Springel V., et al., 2005, *Nature*, **435**, 629
 Taylor E. N., et al., 2011, *MNRAS*, **418**, 1587

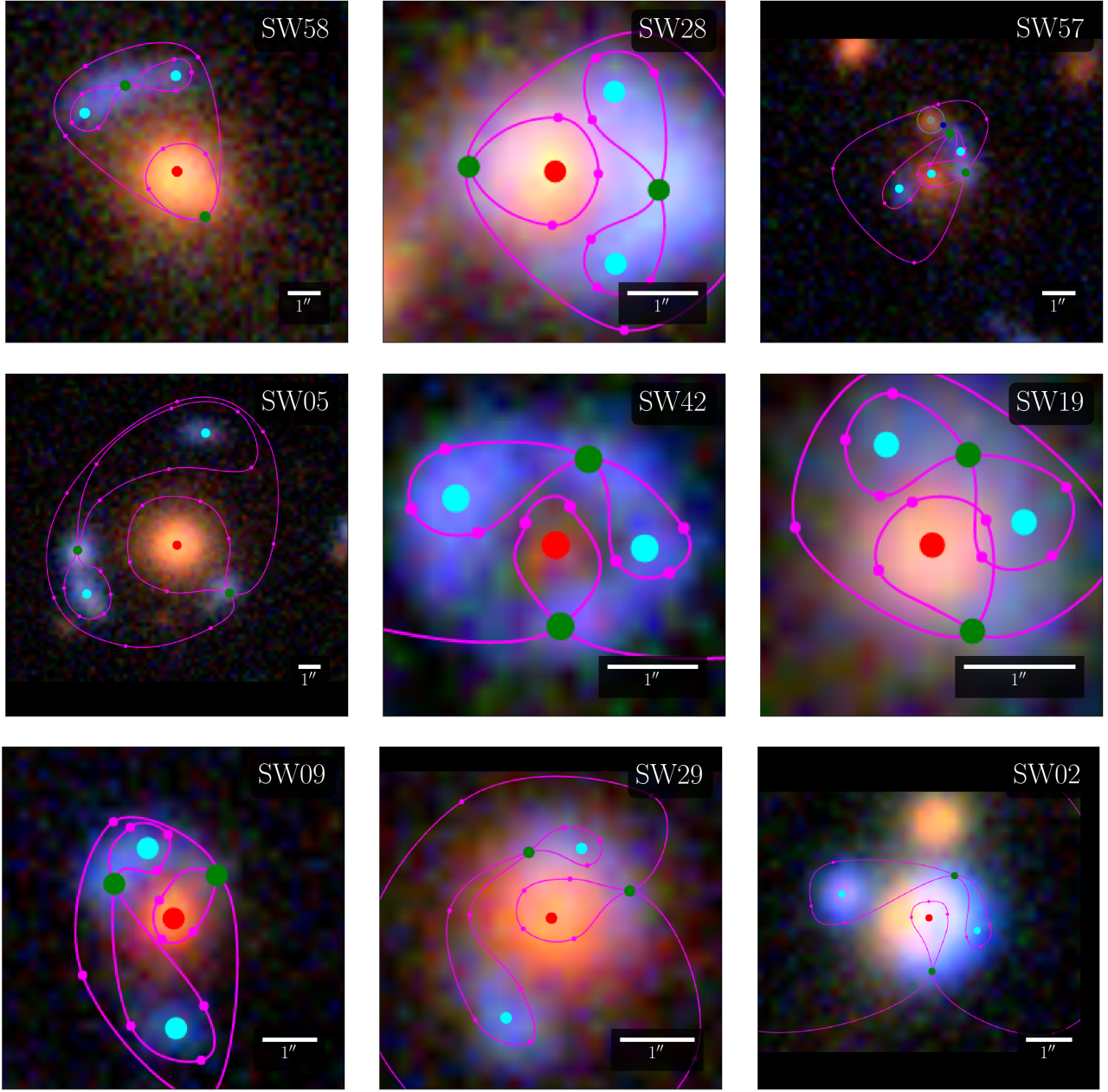


Figure 1. Nine of the lens candidates marked up with spaghetti diagrams. Red, blue and green dots are proposed locations for maxima, minima and saddle points of the arrival time respectively. The curves help guide the placement of the dots, but their precise appearance has no significance. These images are screenshots from the SpaghettiLens user interface, which applies interpolation to background images. The scaling is adjusted to fit the other images. This selection includes the best-modelled systems, but also one case (SW57 at upper right) of unsuccessful modelling. Since the modelling process is collaborative among the volunteers, with anyone welcome to contribute new models or modify existing ones, there are variant spaghetti diagrams for all the modelled systems. The online supplement displays all the models presented for discussion during this work.

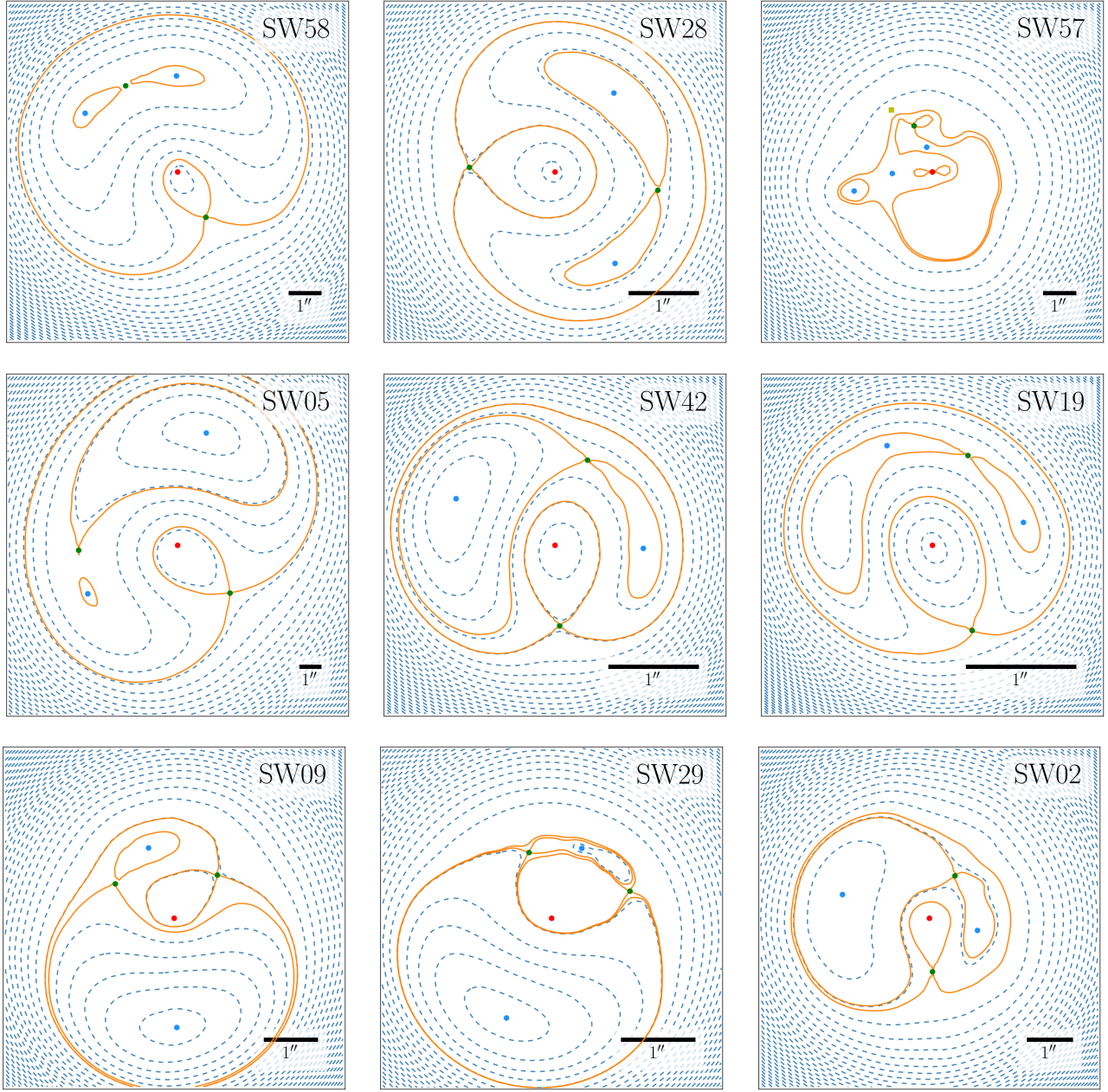


Figure 2. Arrival-time surfaces for models of the systems from Figure 1. The registration differs slightly from Figure 1, but the coloured dots represent exactly the sky positions specified in the earlier figure. The orange contours only qualitatively resemble the earlier pink curves, as they are now precise saddle-point contours from lens models.

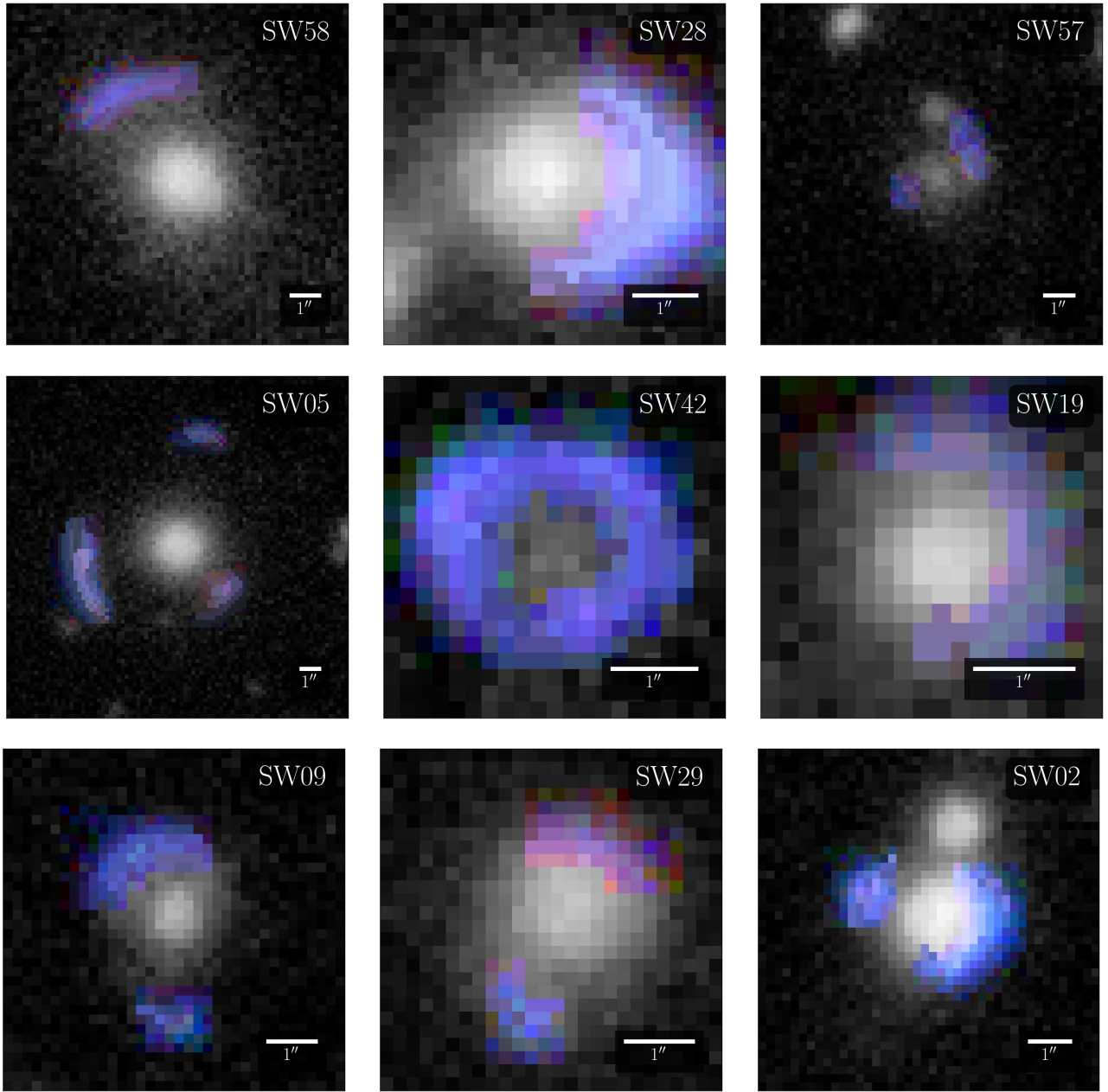


Figure 3. Synthetic images of the systems from Figure 1, derived from the lens models. The reconstructed lensed features keep the Space Warps false-colour scheme from Figures 1. The rest has been changed to black-and-white.

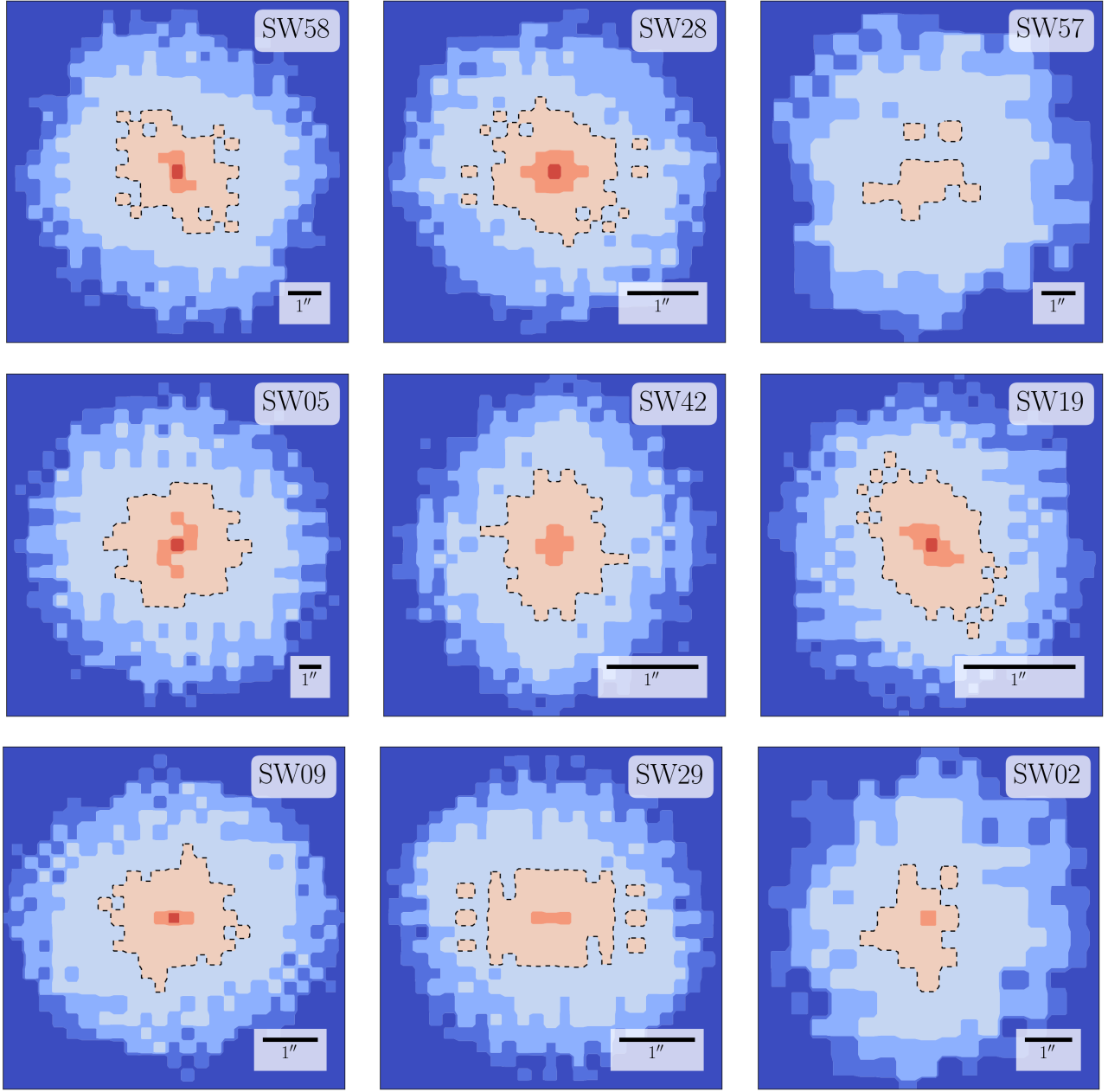


Figure 4. Ensemble-average mass distribution κ for which the results Figures 2–3 were derived. The dashed curves denote $\kappa = 1$. Most of the mass maps have a 180° -rotation symmetry, which is imposed by default. For SW02 and SW57, where the lensing mass is clearly asymmetric, the modeller chose to turn off the symmetry.

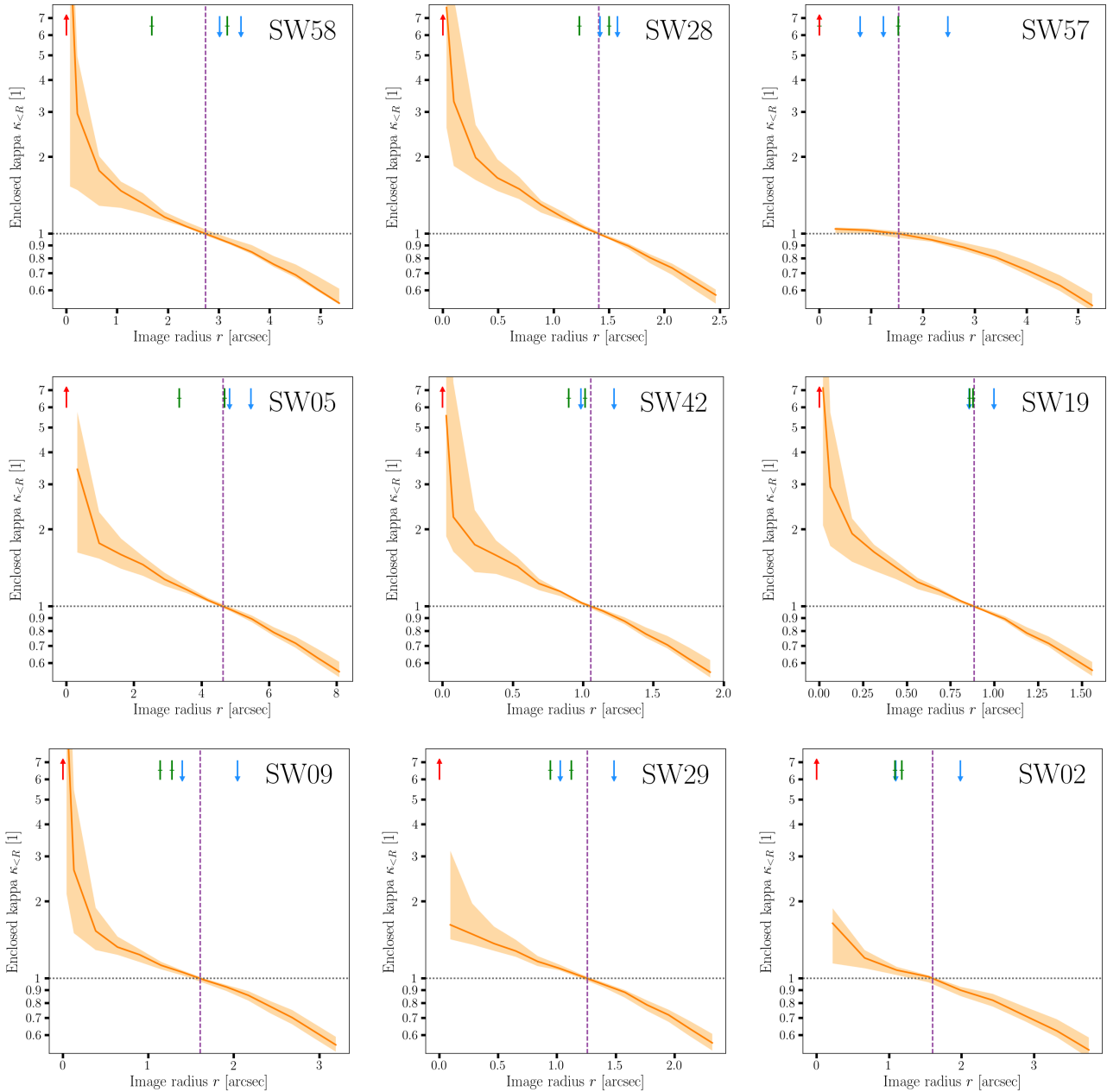


Figure 5. Cumulative circular-averages of the mass maps from Figure 4, with uncertainties. More precisely, we show the enclosed mass within a given projected radius, expressed as the mean κ with a given number of arcsec from the centre of the lensing galaxy. The orange bands refer to the full ensemble of mass maps for the models, while the red curves show the ensemble averages. The dashed vertical line indicates the notional Einstein radius, or where the mean enclosed κ is unity. The short vertical arrows marks the positions of the images (maxima, saddle points and minima).

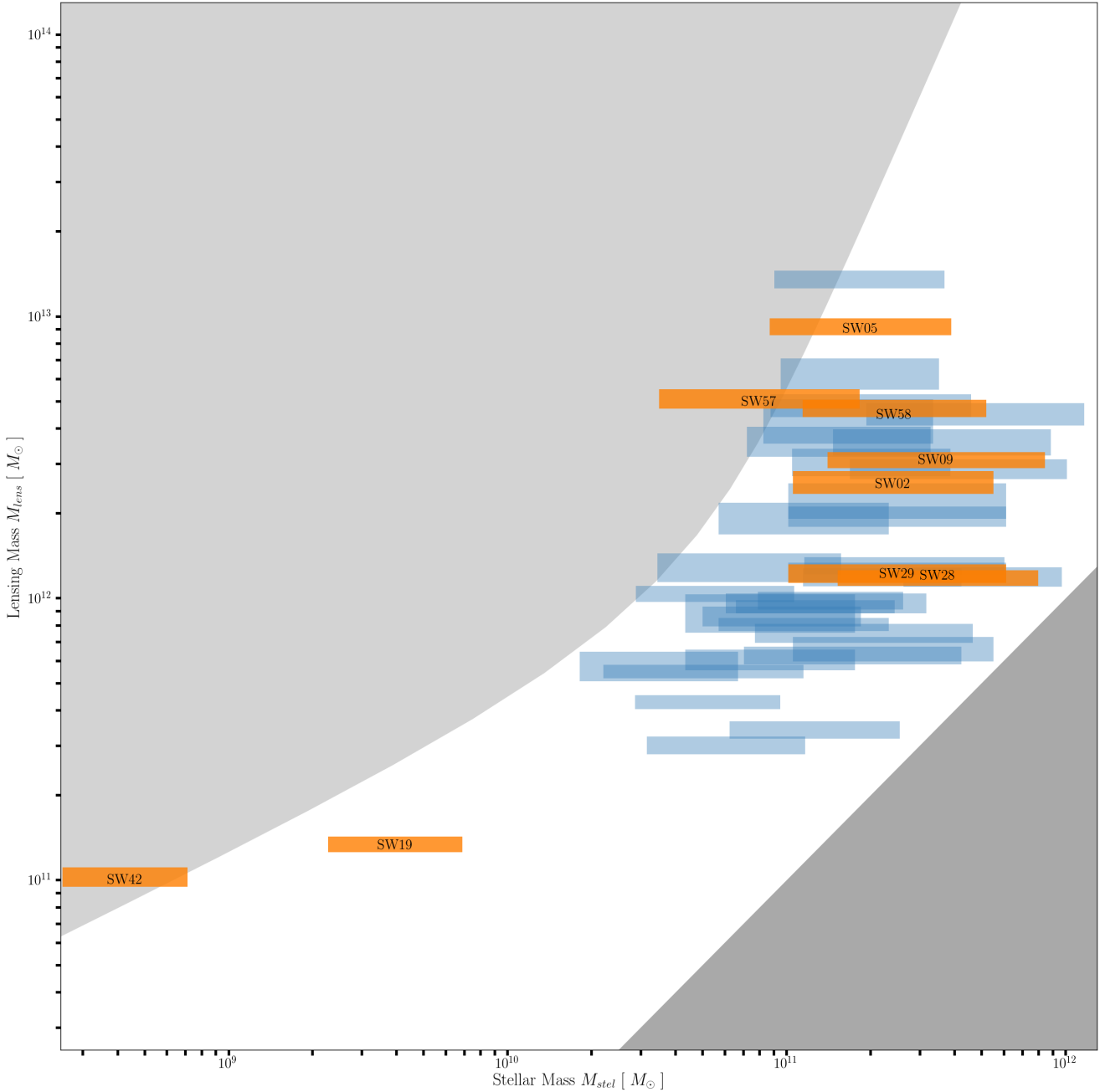


Figure 6. Total mass in the model against the estimated stellar mass, alongside the values for the whole sample. (The labelled orange bars are the systems shown in detail in Figures 1–5.) The horizontal extent of each bar indicates the extreme cases of a young (0.5 Gyr-old) stellar population and the oldest possible population at the given redshift. The vertical extent indicates the spread of masses in lens-model ensemble. The lower-right shaded region is unphysical according to the stellar-population models, because it gives $M < M_{\text{stel}}$. The upper-left shaded region is unphysical according to abundance matching (see Section 4) because it gives $M > M_{\text{halo}}$. That is to say, the unshaded region is $0 < \mathcal{H} < 1$.

Table 1. Diagnostics of a selected model for each Space Warps candidate (see Section 5).

SWID	ZooID	CFHTLS Name	z_{lens}	unblended images	all images discernible	isolated lens	image morphology	synthetic image reasonable	mass map reasonable	$\log_{10} \frac{M_{\text{rel}}}{M_{\odot}}$	$\log_{10} \frac{M_{\text{lens}}}{M_{\odot}}$	halo-matching index \mathcal{H}
SW01	ASW0004dv8	J022409.5–105807	–	✗	✗	✗	SQ	✓	✓	–	–	–
SW02	ASW000619d	J140522.2+574333	0.7	✗	✓	✗	LQ	✓	✓	11.4	12.4	0.47
SW03	ASW0006mea	J142603.2+511421	–	✓	✗	✗	D	✓	✓	–	–	–
SW04	ASW0009cjs	J142934.2+562541	0.5	✓	✓	✗	CQ	✗	✓	11.3	13.1	0.93
SW05	ASW0007k4r	J143454.4+522850	0.58	✓	✓	✓	IQ	✓	✓	11.3	13.0	0.83
SW06	ASW0008swn	J143627.9+563832	0.5	✗	✓	✓	LQ	✓	✗	11.1	11.9	0.46
SW07	ASW0007e08	J220256.8+023432	–	✓	✓	✗	D	✓	✓	–	–	–
SW08	ASW0009qed	J020648.0–065639	0.8	✓	✓	✗	D	✓	✓	11.4	12.3	0.40
SW09	ASW0002asp	J020832.1–043315	1.0	✗	✓	✓	SQ	✓	✓	11.5	12.5	0.40
SW10	ASW0002bmc	J020848.2–042427	0.8	✓	✗	✓	D	✗	✗	11.3	11.9	0.29
SW11	ASW0002qtn	J020849.8–050429	0.8	✗	✓	✗	LQ	✓	✓	11.2	11.8	0.29
SW12	ASW0003wsu	J022406.1–062846	0.4	✓	✓	✗	D	✓	✓	10.8	11.5	0.44
SW13	ASW00047ae	J022805.6–051733	0.4	✗	✗	✗	LQ	✗	✗	11.1	11.9	0.46
SW14	ASW0004xjk	J023123.2–082535	–	✗	✗	✗	SQ	✗	✓	–	–	–
SW15	ASW0004nan	J084841.0–045237	0.3	✗	✓	✗	LQ	✓	✓	10.7	11.6	0.59
SW16	ASW0009bp2	J140030.2+574437	0.4	✗	✗	✓	D	✗	✓	11.3	12.1	0.34
SW17	ASW0005rnb	J140622.9+520942	0.7	✓	✗	✗	D	✗	✓	11.1	12.0	0.44
SW18	ASW0007hu2	J143658.1+533807	0.7	✓	✗	✓	D	✗	✗	11.4	12.1	0.31
SW19	ASW0001ld7	J020642.0–095157	0.2	✗	✓	✗	IQ	✗	✓	9.6	11.1	0.84
SW20	ASW0002dx7	J021221.1–105251	0.3	✓	✓	✓	IQ	✗	✓	11.2	12.0	0.44
SW21	ASW0004m3x	J022533.3–053204	0.5	✓	✗	✗	D	✗	✓	11.1	11.5	0.24
SW22	ASW0009ab8	J022716.4–105602	0.4	✗	✗	✗	D	✗	✓	11.7	12.1	0.15
SW23	ASW0003r61	J023008.6–054038	0.6	✗	✓	✗	SQ	✗	✓	11.2	12.6	0.71
SW24	ASW00050sk	J023315.2–042243	0.7	✗	✓	✗	LQ	✓	✓	11.4	11.8	0.19
SW25	ASW00007mq	J090308.2–043252	–	–	–	–	–	–	–	–	–	–
SW26	ASW0005ma2	J135755.8+571722	0.8	✓	✗	✓	D	✗	✗	11.4	12.3	0.43
SW27	ASW0006jh5	J141432.9+534004	0.7	✗	✗	✗	LQ	✗	✓	10.7	11.7	0.67
SW28	ASW0007xrs	J143055.9+572431	0.7	✗	✓	✗	LQ	✓	✓	11.5	12.1	0.23
SW29	ASW0008qsm	J143838.1+572647	0.8	✗	✓	✓	SQ	✓	✓	11.4	12.1	0.31
SW30	ASW0002p8y	J021057.9–084450	–	✓	✗	✗	IQ	✗	✗	–	–	–
SW31	ASW00021r0	J021514.6–092440	0.7	✗	✓	✓	LQ	✓	✓	11.3	12.7	0.65
SW32	ASW0004iye	J022359.8–083651	–	✗	✓	✗	IQ	✓	✓	–	–	–
SW33	ASW0003s0m	J022745.2–062518	0.6	✓	✓	✗	D	✗	✓	10.9	12.1	0.77
SW34	ASW00051ld	J023453.5–093032	0.5	✗	✗	✓	D	✗	✓	10.9	11.9	0.59
SW35	ASW0004wg	J084833.2–044051	0.8	✗	✓	✗	LQ	✓	✓	11.4	12.1	0.32
SW36	ASW000096t	J090248.4–010232	0.4	✓	✓	✗	D	✗	✓	11.0	12.0	0.56
SW37	ASW00086xq	J143100.2+564603	–	✗	✗	✓	SQ	✓	✓	–	–	–
SW38	ASW0009cp0	J143353.6+542310	0.8	✗	✓	✓	LQ	✓	✓	11.6	12.6	0.42
SW39	ASW0005qiz	J220215.2+012124	–	–	–	–	–	–	–	–	–	–
SW40	ASW0008wmr	J221306.1+014708	–	✗	✓	✓	SQ	✓	✓	–	–	–
SW41	ASW0008xbu	J221519.7+005758	0.4	✓	✗	✓	IQ	✓	✓	10.5	11.8	0.80
SW42	ASW00096rm	J221716.5+015826	0.1	✓	✓	✓	IQ	✓	✓	8.6	11.0	1.04
SW43	ASW0001c3j	J020810.7–040220	1.0	✗	✗	✗	IQ	✗	✓	11.6	12.4	0.34
SW44	ASW0002k40	J021021.5–093415	0.4	✓	✓	✗	D	✓	✓	11.3	12.8	0.76
SW45	ASW00024id	J021225.2–085211	0.8	✗	✓	✓	CQ	✗	✓	11.7	12.6	0.37
SW46	ASW00024q6	J021317.6–084819	0.5	✓	✓	✗	D	✓	✓	10.9	11.8	0.49
SW47	ASW0003r6c	J022843.0–063316	0.5	✓	✗	✓	D	✗	✓	11.2	12.6	0.71
SW48	ASW0000g95	J090219.0–053923	–	✓	✗	✓	D	✓	✓	–	–	–
SW49	ASW00007ls	J090319.4–040146	–	–	–	–	–	–	–	–	–	–
SW50	ASW00008a0	J090333.2–005829	–	✓	✗	✓	LQ	✓	✓	–	–	–
SW51	ASW0006eo0	J135724.8+561614	–	✓	✓	✗	D	✗	✓	–	–	–
SW52	ASW0006a07	J140027.9+541028	–	✓	✗	✓	LQ	✓	✓	–	–	–
SW53	ASW0007vl	J141518.9+513915	0.4	✓	✗	✓	D	✗	✓	11.3	12.5	0.56
SW54	ASW0007sez	J142620.8+561356	0.5	✗	✓	✗	CQ	✓	✓	11.1	12.3	0.68
SW55	ASW0007t5y	J142652.8+560001	–	✗	✓	✓	CQ	✓	✗	–	–	–
SW56	ASW0007pga	J142843.5+543713	0.4	✓	✗	✓	D	✗	✗	10.7	12.0	0.80
SW57	ASW0008pag	J143631.5+571131	0.7	✗	✓	✗	LQ	✗	✗	10.9	12.7	1.08
SW58	ASW0007iwp	J143651.6+530705	0.6	✗	✗	✓	SQ	✓	✓	11.4	12.6	0.58
SW59	ASW00085cp	J143950.6+544606	–	✓	✗	✓	D	✓	✓	–	–	–

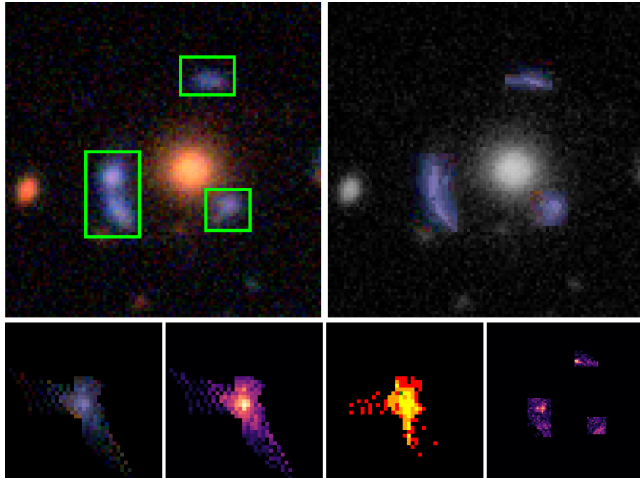


Figure A1. Synthetic lensed image with source-profile fitting in SW05 (J143454.4+522850). Top-left: original image, with areas containing lensed images enclosed within green frames. Top-right: synthetic image (coloured arcs) with lensing galaxy and unrelated objects in greyscale. Bottom from left to right: reconstructed source in colour, intensity (greyscale), count of lens plane pixels per source plane pixel, residual of original image to synthetic image.

APPENDIX A: DEVELOPMENTS IN SPAGHETTILENS

A1 Improved synthetic images

The mass maps produced by the current implementation of SpaghettiLens are based on images of point-like features. No information about extended images is used, except in so far as they help the user identify images of point-like features. The synthetic images offered to users are rudimentary, corresponding to conical light profiles (that is, circular light profiles with brightness decreasing linearly with radius).

We have now developed a prototype to improve the generation of synthetic images. Figure A1 illustrates. First, areas containing lensed images are selected (green frames in the figure). The selected areas should be as free as possible from of light from the lensing galaxy or from extraneous objects. Pixels within the selected areas are mapped to a grid on the source plane, using bending angles given by the mass model. The mapping from lens-plane pixels to source-plane grid cells is many-to-one, because of image multiplicity and magnification. The brightness of each source-plane pixel is set to the mean of all the lens-plane pixels mapping to it. Finally, the mapping is run back to the lens plane. The result is a synthetic image. In effect, one is reconstructing a source-plane brightness map by least-squares.

The procedure is not yet implemented in SpaghettiLens but can be applied in post-processing. The new synthetic images could be used to improve the mass reconstruction, by weighting the ensemble of maps according to how good the synthetic images are, but we have not attempted to do so as yet.

A2 Sub-sampling of central region

The models of simulated lenses in Küng et al. (2015) showed a tendency to produce density profiles which were too shallow.

Allowing smaller mass tiles in the central region, thus allowing the mass profile to rise more steeply near the centre, was suggested as a possible cure.

Figure A2 shows an experiment with smaller mass tiles in the inner region. Replacing the very central mass tile with 9 smaller tiles allows for steeper central profiles. Doing the same for the 25 innermost mass tiles allows for still steeper central profiles, eliminating the systematic shallowness. This is, however, still not a completely satisfactory solution, because (a) it increases the number of mass tiles by 40% and significantly increases the computational time, and (b) the square boundary between area with different tile sizes is rather undesirable. The main modelling work in this paper was, however, done before the experiments with smaller mass tiles was complete. Some of the models presented in this paper apply the intermediate option (corresponding to the middle panel in Figure A2) while others use the old system. The results in this paper, however, mainly concern the enclosed mass in the outer regions, so shallowness in the central region should be inconsequential.

A3 Parameterisation of pixel models

In order to fit the set of pixelated models to a single parameterised model, a program was written that took a parameterised function and subtracted from it the mean and the principal components of the data, which were calculated using classical Principal Component Analysis. This created the residuals function. The number of components used in the analysis was varied, to test how this affected the output, and it was found that using 5 principal components tended to give a reasonable approximation. A masking function was added which selected only the data points that fell inside the image of the lens, and the principal components were clipped in order to keep the values inside the region of the ensemble of models. Any value higher than the clip was set to be the clip value. This was chosen to be 2.5 as, assuming that the data follows a Gaussian error distribution, almost all the values for the variance should lie between 2 and 3 standard deviations from the mean. Minimising the residuals function produces the set of parameters that fit the parameterised function to the original pixelated ensemble most closely. A least squares fit was used to perform this minimisation. The parameterised model function was obtained from the gravitational potential of an isothermal ellipsoid mass distribution (Keeton 2001). This model is frequently used to describe gravitational lenses as it tends to fit well with observations. The isothermal ellipsoid model outputs three useful parameters: the radius of the Einstein ring, the ellipticity of the model and the angle of the ellipticity from the vertical, giving the orientation of the galaxy. By applying this model to simulated lenses for which the values of these parameters were already known, it was possible to gain an estimate of the projected accuracy of the results, before applying the model to the candidate lensing galaxies.

Preliminary results on recovery of Einstein radii are shown in Figure A3.

This paper has been typeset from a Te_X/L_AT_EX file prepared by the author.

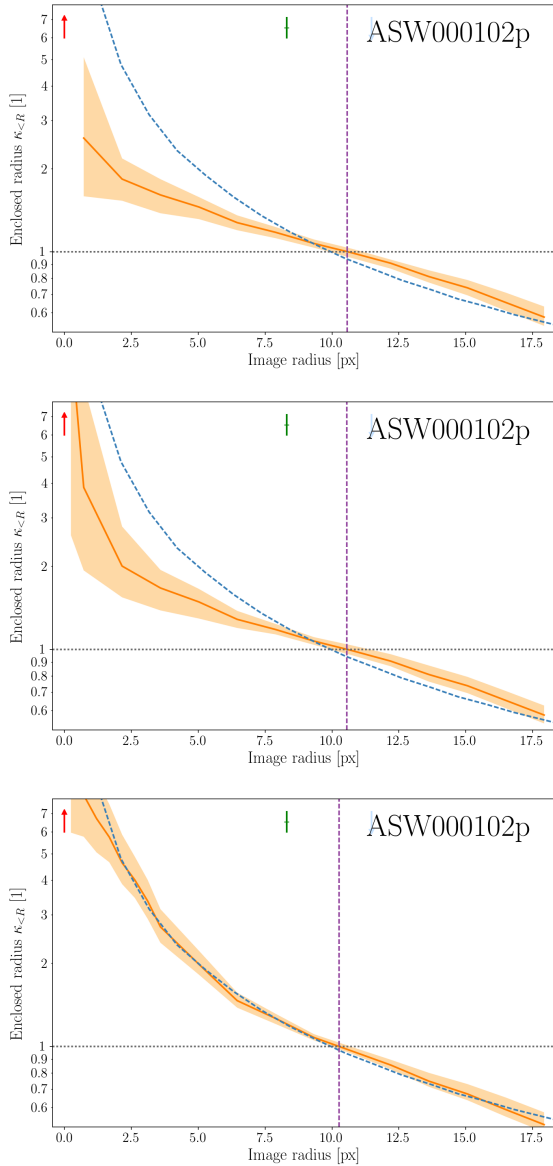


Figure A2. Model improvement resulting from using smaller mass tiles in the inner region of the mass model. Shown here are the average enclosed κ within a given projected radius, for three different reconstructions of a simulated lens (sim) from Space Warps. In each panel, the dashed blue curve is the correct answer. The orange band represents the statistical ensemble from SpaghettiLens, the orange line being the ensemble mean. Locations of images (maximum, saddle point, minimum) are marked with vertical arrows. Crossing the horizontal $\kappa = 1$ line is the effective Einstein radius r_E . The upper panel is from Küng et al., (2015) (see Figure 3 of that paper). The middle panel is the result when the innermost mass tile is replaced by 9 smaller tiles. The lower panel results from replacing each of the innermost 5 by 5 tiles each with 9 smaller tiles.

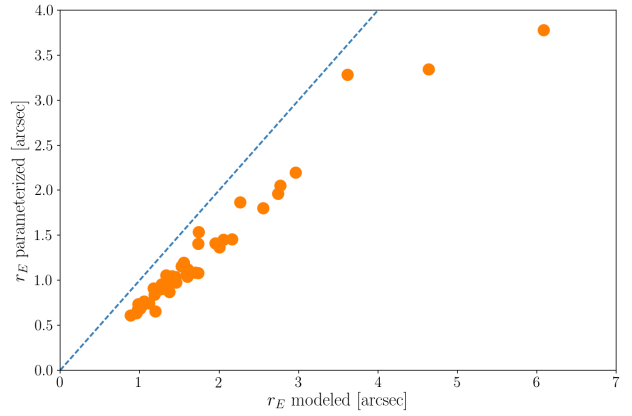


Figure A3. Comparison of Einstein radii r_E obtained from mass tiles directly to those obtained from a parameterized model to test the performance of the parametrisation algorithm. The parameterized model was generated using principle component analysis on the ensemble of models. The blue dashed line represents a perfect recovery of r_E .